Personalized Visual Simulation and Objective Validation of Low-Order Aberrations of the Human Eye

Matheus L. Krueger, Manuel M. Oliveira
Institute of Informatics, UFRGS, Porto Alegre, Brazil
Email: {matheus.krueger, oliveira}@inf.ufrgs.br

Airton L. Kronbauer
CORS, Porto Alegre, Brazil
Email: ak@cors.med.br

***Abstract*—We present a practical approach for personalized simulation and objective validation of the effects of low-order aberrations (*i.e.*, myopia, hyperopia and astigmatism) on optical systems, such as the human eye. We characterize the optical aberrations using a wavefront aberration function derived from one's eyeglasses or contact lenses prescription data, expressed in terms of Zernike polynomials. Given the prescription data, a target image at known distance from the subject, and a specified pupil size, the simulation efficiently computes the corresponding aberrated view. We validate the quality of our simulations using ground truth data captured by a camera with the same kind of aberrations. For validation, we use three objective metrics: structural similarity (SSIM), peak signal-to-noise ratio (PSNR), and absolute pixelwise differences (AD) between the simulated images and the ones captured by the camera with induced aberrations. Our results achieved a SSIM mean value of 0.93 (minimum of 0.91) and a PSNR mean value of 35.50 dB (minimum of 29.50 dB), showing that they are structurally similar and virtually indistinguishable from the ground truth images captured by the camera.**

***Keywords*-Personalized Visual Simulation; Low-order Aberrations; Fourier Optics; PSF**

I. Introduction

Vision is the primary channel we use to perceive the universe. It allows us to acquire information about the surrounding world by sensing the intensity and color of light. This is a personal experience, as the perceived image is affected by several individual factors (*e.g.*, refractive errors, light sensitivity, distribution of photoreceptors in the retina, etc.). Thus, a tentative to simulate the full visual experience would require the integration of a wide range of subjects, including optics, anatomy, physiology, biochemistry, psychology, and neurosciences [1].

Low-order visual aberrations (*i.e.*, myopia, hyperopia, astigmatism, and presbyopia) can be described in terms of sphero-cylindrical values and can be corrected with the use of eye glasses or contact lenses. They are responsible for about 90% of one's loss of visual acuity [2]. The remaining 10% loss is due to a combination of particular eye imperfections, known as *high-order aberrations* (*e.g.*, trefoil, coma, quadrafoil, secondary astigmatism). Visual aberrations can be described by the eye's point-spread function (PSF), often represented using wavefront maps. Fig. 1 illustrates the human eye and the effects of some low-order aberrations. From a simple geometrical perspective, when an eye is misfocused at a point in the scene, the light emitted/reflected by such a point is spread out across some area (circle of confusion) of the retinal surface, causing blur (Fig. 1(b) and 1(c)). If the eye is well focused at a scene point, such point maps to a point on the retina (Fig. 1(a)).

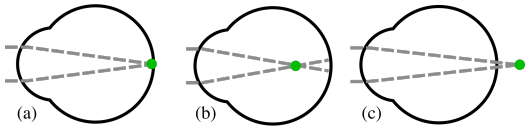

Figure 1. The human eye and some low-order aberrations. (a) A perfect eye focuses a set of parallel rays to a single point on the retina; (b) a myopic eye has an elongated eye ball or a bumped cornea, focusing parallel rays at a point before the retina; and (c) a hyperopic eye has a shallow eye ball or a flatter cornea, thus focusing parallel rays at point behind the retina. The conditions described in (b) and (c) lend to blurred vision.

Unlike traditional 2-D digital image processing, in which an image is blurred by a convolution with a spatially-invariant low-pass filter kernel, visual blurring is a depth-dependent phenomenon (*i.e.*, the amount of blurring introduced by the eye's PSF varies with the distance from the observer to the scene element). If depth is not taken into account by the blurring method, the resulting image might be very different from the one formed onto the retina.

We present a practical approach for personalized simulation and validation of the effects of low-order aberrations on optical systems, such as the human eye. Our approach is based on Fourier optics tools and assumes that target images are planar and perpendicular to one's eye sight, just like Sloan charts used in typical vision acuity tests. Although the examples shown in the paper consist of monochromatic images (eye chart optotypes), the extension to color images is straightforward. We demonstrate the effectiveness of our technique through comparisons against ground truth data acquired using a DSLR camera with induced low-order aberrations. For validation, we use three objective metrics: structural similarity (SSIM) [27], peak signal-to-noise ratio (PSNR), and absolute pixelwise differences (AD). The results show that our simulations are structurally similar and virtually indistinguishable from the ground truth images captured by the camera.

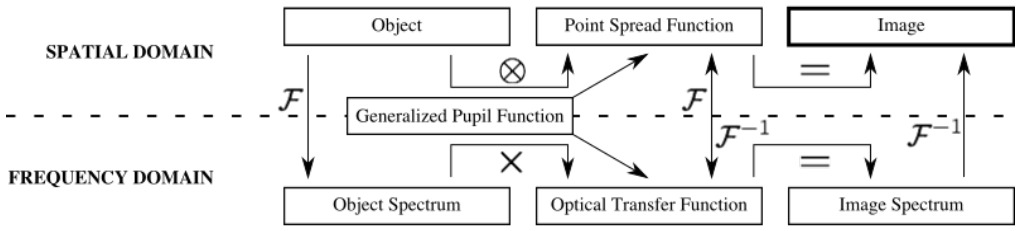

Figure 2. The pipeline for simulating visual aberrations. It illustrates two paths for computing the retinal image of an object when the point spread function of the eye (PSF), or equivalently, the optical transfer function (OTF), is known. The computation indicated at the top is carried out entirely in the spatial domain. The convolution of image with the PSF gives the retinal image directly. The more efficient computation in the spatial frequency domain is illustrated at the bottom. In that case, the product of the object spectrum (obtained by the Fourier transform of the object) and the optical transfer function is the image spectrum, from which the image itself can be obtained by inverse Fourier transformation. $\mathcal{F}$ and $\mathcal{F}^{-1}$ stands for the Fourier transform and inverse Fourier transform operators.

II. Related work

Vision simulation has been addressed in different ways over the years. Since the first computer-generated depth-of-field images by Potmesil and Chakravarty [3], there has been a significant number of computer graphics techniques addressing the rendering of realistic effects. More recently, the possibility of estimating and compensating for refractive errors has attracted the attention of several researchers, mainly addressing the formulation of interactive, portable, and inexpensive solutions. The following subsections describe the main techniques for simulating, estimating, and correcting visual aberrations.

A. Optical Simulation Techniques

Barsky [4] proposed a method for generating synthetic images incorporating the optical characteristics of an individual. Specifically, his method simulates the perception of an individual based on data acquired using a Shack-Hartmann wavefront aberrometer. Once the wavefront data is captured, it is sampled and used to blur the input synthetic scene at different depths. Yu [5] presented a technique for simulating views of synthetic and real scenes focusing at a specific depth. The author also relies on data captured by a Shack-Hartmann aberrometer to construct a wavefront, which is used to blur a sharp image according to a depth map. Yu did not provide validation for his simulations.

Several researchers have used raytracing techniques and anatomical optics to study and simulate vision by using theoretical models of the human eye [6], [7], [8]. Camp et al. [6] described two ray tracing algorithms for deriving an optical PSF from corneal topography measurements. They focused on simulating and evaluating optical performance of patients' eyes with the following corneal pathologies: *keratoconus*, *epikeratophakia for aphakia* and *radial keratonomy*. Kolb et al. [7] presented a physically-based camera model that simulates aberration and radiation. To simulate such effects, they compute the geometry of image formation of a particular lens system using a modified distributed ray tracing algorithm. The algorithm is a hybrid of rendering and lens-maker techniques, and can produce images of synthetic scenes showing a variety of optical effects. Mostafawy et al. [8] combined the algorithm presented by Kolb et al. and the dimensions of an schematic eye model to generate virtual simulations of vision after corrective surgery. Unlike these techniques, our approach does not rely on ray tracing, but uses Fourier optics to model visual aberrations. In a work developed concurrently to ours [9], Watson [10] describes a Mathematica implementation for computing the human eye PSF based on descriptions found in Goodman [11] and Dai [12]. Unlike our work, however, Watson does not provide an objective validation for his simulations.

B. Non-Optical Simulation Techniques

Some techniques are concerned with non-optical effects. Deering [13] describes a photon-accurate model of the human retina. It is used with computer graphics techniques and a simplified optical model of the eye to produce synthetic simulations of the image formation process.

Ritschel et al. [14] addressed the problem of glare rendering and proposed a model for real-time dynamic simulation of light scattering in the human eye. The authors have performed psychophysical studies to measure the perception of brightness for glare models. However, they state that, as any other intrinsic phenomena, no ground truth can be obtained. The model validation remains a challenging task.

C. Estimating/Correcting Visual Optical Aberrations

Pamplona et al. [15] presented an approach for estimating low-order aberrations on a smartphone by performing interactive alignments of patterns. Kronbauer et al. [16] developed a psychophysical approach for vision measurement in candelas. It consists of displaying light stimuli for a patient to determine his/her absolute threshold for lit and dark conditions. They found some strong correlation between visual acuity and the absolute threshold.

Many methods have tried to free the viewer from the need of optical correction when observing displays [17], [18], [19], and printings or projections [20]. Other works have

explored physiologically-based models to provide insights and feedback on how to produce high-fidelity effects and improve visualization experiences [21], [22], [23].

III. Personalized Visual Simulation of Low-Order Aberrations

Since we are primarily interested in visual acuity, all experiments and discussions presented here are based on monochromatic images. The extension to color images is straightforward and explained in Section III-C. As visual blurring is a depth-dependent phenomenon, we have adopted the simplifying assumption that the observed images are at some constant depth. For this, we use two sets of charts containing standard Sloan letters: black letters on white background, as well as white letters on black background.

A. Target Images and Capture Setup

We have created images of Sloan letters at LogMAR (Logarithm of the Minimum Angle of Resolution) values ranging from -0.3 to 1.0 in steps of 0.1. The LogMAR scale [24] provides a more accurate estimate of visual acuity when compared to other charts (*e.g.*, Snellen), being the recommended one for research settings. Our target images were created according to Eq. 1 for testing vision from three feet away. The individual letters were rendered using the vector graphics capabilities of Inkscape and the Sloan PostScript fonts provided by Pelli et al.[25]. At the prescribed distance, the ratio between one pixel (of a Canon EOS Rebel T3 camera) and one arc minute is 1:1, that is, the letters with a LogMAR value of 0 (or the known Snellen fraction 20/20) are exactly 5 pixels tall. For the purpose of our simulations, each black (white) optotype was placed against a 113×113-pixel black (white) square. Since 1 degree corresponds to 60 arc minutes, each such square covers a total field of view (FOV) of $1.88^\circ \times 1.88^\circ$. The conversion from *Snellen decimal acuity* values to LogMAR values is presented in Eq. 2. A Snellen decimal acuity value is the decimal representation of the Snellen fraction (*e.g.*, Snellen ratios of 20/20 and 20/40 correspond to Snellen decimal acuity values of 1.0 and 0.5, respectively).

$$\begin{aligned} letter\ size_{mm} = tan\left(deg2rad\left(\frac{5}{60}\right)\right) \\ \times (chart\ distance_{mm}) \\ \times (10^{-LogMAR})^{-1} \end{aligned} \tag{1}$$

$$LogMAR = -\log_{10}(Snellen\ decimal\ acuity) \tag{2}$$

We have printed the described white- and black-background LogMAR charts containing Sloan letters specifically designed for a viewing distance of three feet. The charts were printed on white paper using a laser printer at 360 dpi. We then took pictures of the charts with a Canon EOS Rebel T3 DSLR camera. The camera was placed at three feet (91.44 cm) from the chart, with focal length set to 18mm. Since images acquired using this setup respect the 1:1 ratio between pixels and arc minutes, one can crop the squares containing each optotype for further processing.

B. Modeling Visual Aberrations

We characterize the optical aberrations of the human eye using a wavefront aberration function. Such a function defines a wavefront map, which is approximated using Zernike polynomials. They consist of a series of orthogonal polynomials over the area of a unitary circle and can be expressed either in Cartesian (x,y) or polar (θ, ρ) coordinates. Obtaining a complete wavefront function, which models both low-order and high-order aberrations, requires access to expensive wavefront aberrometer devices. In this work, we only consider the low-order aberrations since they can be easily obtained from any eyeglass or contact lens prescriptions. One should note, however, that low-order aberrations alone are responsible for about 90% of one's total loss of visual acuity [2]. This should not come as a surprise, given that eyeglasses can only correct for low-order aberrations and are the primary way of achieving corrected 20/20 vision.

We obtain wavefront aberration function $W_{(x,y)}$ from prescription data as [12]:

$$W_{(x,y)} = \sum_{i=-1}^{1} c_2^{2i}\ Z_2^{2i}{}_{(x,y)}, \tag{3}$$

where

$$\begin{aligned} c_2^{-2} &= \frac{R^2\ C\ \sin(2\theta)}{4\sqrt{6}} & Z_2^{-2}{}_{(x,y)} &= xy\sqrt{\frac{6y^2}{x^2}+6} \\ c_2^{0} &= -\frac{R^2\ (S+C/2))}{4\sqrt{3}} & Z_2^{0}{}_{(x,y)} &= \sqrt{3}(2x^2+2y^2-1) \\ c_2^{2} &= \frac{R^2\ C\cos(2\theta)}{4\sqrt{6}} & Z_2^{2}{}_{(x,y)} &= x^2\sqrt{\frac{6y^2}{x^2}+6} \end{aligned}$$

and c_2^{-2}, c_2^0, and c_2^2 are the coefficients of the Zernike polynomials corresponding to *oblique astigmatism* (Z_2^{-2}), *defocus* (Z_2^0), and *vertical astigmatism* (Z_2^2), respectively. S, and C are, respectively, the *sphere* and *cylinder* values from the prescription, specifying the optical powers in diopters (D). ϕ is cylinder axis expressed in degrees. The values S, C, and ϕ are popularly referred to as the "degree", the "astigmatism", and the "axis of astigmatism", respectively. R is the radius of the subject's pupil (an aperture, in general) measured in mm, and c_2^{-2}, c_2^0 and c_2^2 are in μm. Fig. 3 illustrates a wavefront map obtained for $S = 0.5$D, $C = -2.0$D, $\phi = 45^\circ$ and $R = 1.5$mm. If no aberration is present, the resulting wavefront is planar.

C. Image Filtering

Given S, C, R, and ϕ, one can obtain the effective aberration function as $kW_{(x,y)}$, where k is the spherical wavenumber (*i.e.*, $k = 2\pi/\lambda$), and $W_{(x,y)}$ is the wavefront

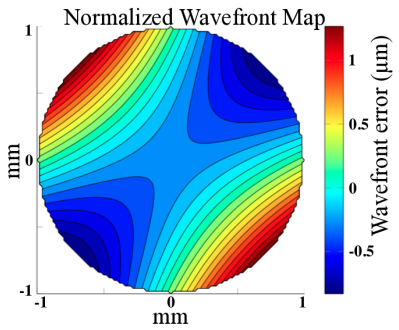

Figure 3. Normalized wavefront aberration contour map for an eye with: S = 0.5D, C = -2.0D, $\phi = 45°$ and R = 1.5mm. The circle represents a 1.0mm-radius crop of the 1.5mm pupil. The root mean square (RMS) wavefront error (in μm) is the deviation of the wavefront aberration function W (Eq. 3) from a plane wave.

aberration function expressed using the Zernike polynomials. For the case of low-order aberrations, $W_{(x,y)}$ is defined by Eq. 3, which takes into account oblique astigmatism, defocus, and vertical astigmatism. $\lambda = 550nm$ is a standard wavelength used for monochromatic simulation [12]. For color images, the filtering process needs to be performed separately for each channel, using a different λ value for each of the RGB channels (*i.e.*, $\lambda_R = 700nm$, $\lambda_G = 510nm$, $\lambda_B = 440nm$) [12].

A pupil function $P_{(x,y)}$ is a binary function that evaluates to 1 inside the projected aperture, and 0 outside it. According to Goodman [11], the *generalized pupil function* $\mathbb{P}_{(x,y)}$ is given by:

$$\mathbb{P}_{(x,y)} = P_{(x,y)} \exp[j\, kW_{(x,y)}], \tag{4}$$

where $j = \sqrt{-1}$. Note that $\mathbb{P}_{(x,y)}$ is a complex number. One can obtain the point spread function of the eye (optical system) as the power spectrum of $\mathbb{P}$, *i.e.*, $PSF = |\mathcal{F}(\mathbb{P})|^2$, where $\mathcal{F}$ is the Fourier transform operator. Given the PSF and an input image I, one can compute O (the view of I through the given optical system) as the 2-D convolution $O = PSF \otimes I$. A more efficient computation of O can be obtained in the frequency domain, as illustrated at the bottom of Fig. 2. In that case, $O = \mathcal{F}^{-1}(\mathcal{F}(I) * OTF)$, where $OTF = \mathcal{F}(PSF)$ is the *the optical transfer function* and $*$ is the element-wise multiplication.

D. Experimental Validation Setup

We use a DSLR camera (Canon model EOS Rebel T3 with an 18-55mm zoom lens) in order to represent a perfect eye (*i.e.*, without refractive aberrations). We place additional lenses in front of the camera's optical system to induce low-order aberrations (*i.e.*, myopia, hyperopia, and astigmatism). Such lenses are placed on a support fixed to a UV filter attached to the main lens. Fig. 4(left) shows the camera with an additional +1.0 diopter lens attached to it. The support can hold up to three additional lenses.

For our simulations, we use a simplified eye model adjusted to the camera's settings to achieve consistent results between them. More specifically, we make sure that the *f-number* (*i.e.*, the ratio of the camera lens' focal length f to the diameter D of its aperture):

$$f_{number} = \frac{f}{D} \tag{5}$$

is the same for the camera and the eye model. For the experiments described in the paper, we fixed the focal length of the camera's main lens to 18mm (regardless of the use of additional lenses). Thus, for instance, given *f-number* values of 4.0, 4.5 and 5.0, the corresponding camera lens aperture values are set to 4.5mm, 4.0mm and 3.6mm, respectively. Our simplified eye model (Fig. 4(right)) has an axial diameter of 18mm. The crystalline lens causes the nodal point **N** to be behind the crystalline. Thus, the eye model's effective focal length is 13.5mm: $f_{eye} = 18mm \times \eta_{eye} = 18mm \times 1.333 = 13.5mm$, where η_{eye} is the index of refraction of the eye. As a result, the eye model's pupil size (equivalent to the camera's lens aperture) needs to be rescaled to maintain the same *f-number* value as the camera. Table I shows the corresponding values of the equivalent camera apertures and pupil diameters.

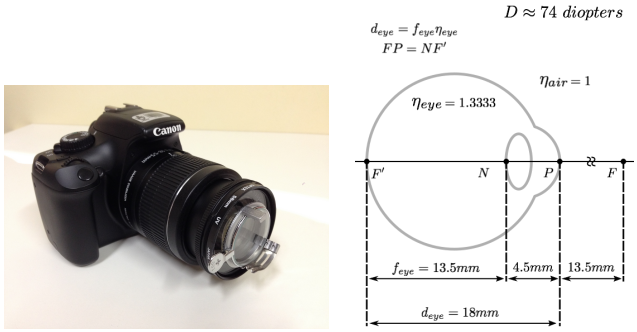

Figure 4. Optical systems used in the setup: (left) Canon EOS Rebel T3 with support for up to three extra lenses. Focal lens set to 18mm. (right) Simplified eye model with effective focal length of 13.5mm. **N** is the nodal point.

Table I
DSLR CAMERA (18MM FOCAL LENGTH) APERTURES AND OUR SIMPLIFIED EYE MODEL (13.5MM FOCAL LENGTH) PUPIL DIAMETERS FOR VARIOUS F-NUMBERS.

f-number	Camera's aperture	Eye's pupil diameter
f/4.0	4.5mm	3.4mm
f/4.5	4.0mm	3.0mm
f/5.0	3.6mm	2.7mm

E. Vertex Distance and Ray Transfer Matrix

The actual optical power of a lens prescribed for correcting low-order aberrations varies according to the distance from the lens to the cornea, also known as *vertex distance*. To compensate for the spacing between the camera's main

lens and the additional ones, we use a *ray transfer matrix* (RTM) formulation [26]. This is modeled as the product of three matrices: a thin lens ($_{TL}$) matrix that approximates the DSLR's optical system by a single thin lens, a distance d propagation matrix, and a thin lens matrix representing our additional lenses:

$$\begin{bmatrix} A_{TL} & B_{TL} \\ C_{TL} & D_{TL} \end{bmatrix} = \begin{bmatrix} 1 & 0 \\ -\frac{1}{f_{cam}} & 1 \end{bmatrix} \begin{bmatrix} 1 & d \\ 0 & 1 \end{bmatrix} \begin{bmatrix} 1 & 0 \\ -\frac{1}{f_{lens}} & 1 \end{bmatrix}$$

$$= \begin{bmatrix} 1 - \frac{d}{f_{lens}} & d \\ \left(\frac{\frac{d}{f_{cam}} - 1}{f_{lens}} - \frac{1}{f_{cam}} \right) & 1 - \frac{d}{f_{cam}} \end{bmatrix} \quad (6)$$

Here, f_{cam} is the DLSR camera focal length (*i.e.*, 18mm in our case), and f_{lens} is the focal length of the (combined set of) additional lens(es). In case of a divergent lens l (*i.e.*, negative diopters), f_{lens} is minus the focal lens of l. The image captured by the resulting optical system is formed at a distance x behind the DSLR camera's optical system. Assuming we want to capture the image of an infinitely far away object (*e.g.*, at distance $s = 10^{20}$mm from the camera), the overall RTM can computed as:

$$\begin{bmatrix} A & B \\ C & D \end{bmatrix} = \begin{bmatrix} 1 & x \\ 0 & 1 \end{bmatrix} \begin{bmatrix} A_{TL} & B_{TL} \\ C_{TL} & D_{TL} \end{bmatrix} \begin{bmatrix} 1 & s \\ 0 & 1 \end{bmatrix} \quad (7)$$

Since a set of parallel rays (of an infinitely far away object) are focused by a lens to its focal point, one concludes that x should indeed be the focal length $f_{cam+lens}$ of the compounded optical system comprised by the camera's main lens plus the additional one. To allow for image formation, it is required that $B = 0$ in the $ABCD$ matrix (Eq. 7) [26]. Thus, one can solve for x, obtaining:

$$x = f_{cam+lens}$$

$$= \frac{(d+s) \times (f_{cam} \times f_{lens}) - (d \times f_{lens} \times s)}{(d - f_{lens}) \times f_{cam} + (f_{cam} + f_{lens} - d) \times s} \quad (8)$$

Since 1 diopter = 1/meter, and $f_{cam+lens}$ is expressed in mm, the dioptric power of the resulting compounding optical system is given by:

$$diopt_{cam+lens} = \frac{1}{f_{cam+lens} \times 10^{-3}} = \frac{10^3}{f_{cam+lens}} D \quad (9)$$

Table II shows the actual increase in dioptric power that result from placing additional lenses with different powers in front of the camera's main lens, considering a vertex distance of $10mm$. Thus, for instance, when placing a +1.0D lens in front of the camera's main lens, we are in fact inducing myopia of 1.0101D. Therefore, to obtain an image comparable to the one captured by the camera, our simulation should compute a wavefront aberration for 1.0101D of myopia.

Table II
ACTUAL INCREASE/DECREASE IN DIOPTRIC POWER OBTAINED BY PLACING ADDITIONAL LENSES WITH VARIOUS POWERS IN FRONT OF THE CAMERA'S MAIN LENS CONSIDERING A VERTEX DISTANCE OF 10MM.

Additional lens	Actual dioptric power	Additional lens	Actual dioptric power
0.0 D	0.0000 D	0.0 D	0.0000 D
1.0 D	1.0101 D	-1.0 D	-0.9901 D
2.0 D	2.0408 D	-2.0 D	-1.9608 D
3.0 D	3.0928 D	-3.0 D	-2.9126 D
4.0 D	4.1667 D	-4.0 D	-3.8462 D

IV. RESULTS

This section compares our simulated results with an optical ground truth, obtained by capturing images of the LogMAR charts. For the examples shown here, a DSLR camera was set up for $f/5.0$ (third row of Table I), although other values could have been used. Whenever we refer to the dioptric power of additional lenses, our simulations account for the values described in Table II.

To evaluate the quality of the simulated results, we use three objective metrics: the structural similarity image metric (SSIM) [27], the peak signal-to-noise ratio (PSNR), and the absolute (pixelwise) difference (AD) between the captured and simulated images. The SSIM metric measures image degradation perceived as change in structural information. It is calculated for each pixel of a given image with respect to some reference image, based on its relationship to other pixels in an 11×11 neighborhood. PSNR, in turn, is a popular metric for assessing the quality of image reconstruction and compression. It is often expressed using a decibel scale, and computed as

$$PSNR = 10 \log_{10} \left(\frac{peakval^2}{MSE} \right), \quad (10)$$

where

$$MSE = \frac{1}{mn} \sum_{i=0}^{m-1} \sum_{j=0}^{n-1} (I_{ref}(i,j) - I(i,j))^2, \quad (11)$$

and I is an image being compared to a reference image I_{ref}, both with the same dimensions $m \times n$. $peakval$ is the maximum possible value for a pixel. For instance, for a grayscale image using 8-bits per pixel, $peakval = 255$.

Figs. 5 and 6 compare images of the letter **N** from the LogMAR charts with white and black background, respectively, captured by the DSLR camera with induced aberration (top row) against the results of our simulations (second row). The images in the top rows were captured by the camera with additional lenses, ranging from 0 to -4 diopters (Fig. 5) and from 0 to +4 diopters (Fig. 6), in steps of 1 diopter. The second rows show the images produced using our simulation considering the adjustments in dioptric power required to account for the 10mm spacing between the camera's main lens and the additional one (Table II). Our

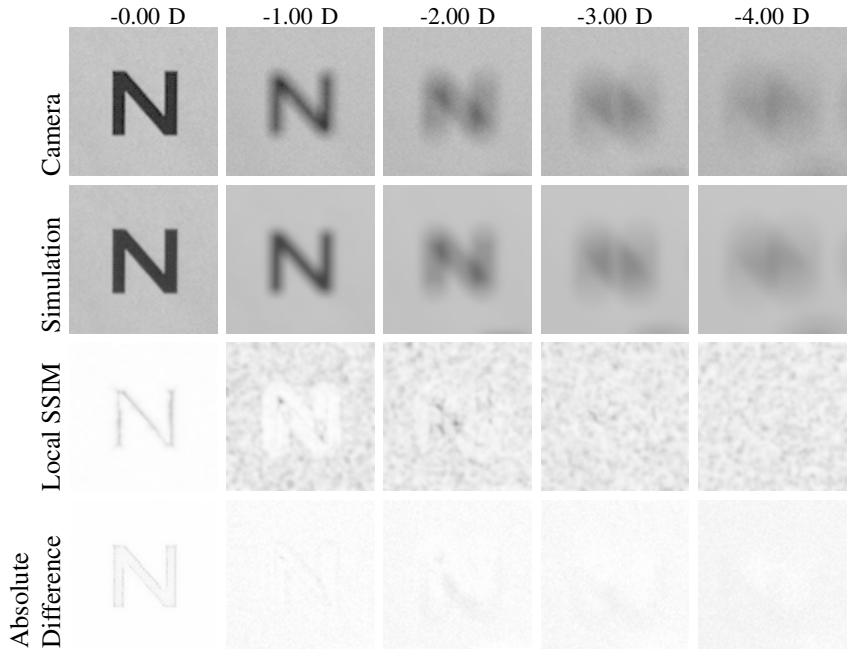

Figure 5. Comparisons of our simulated results against ground truth obtained with a hyperopic camera. These large images correspond to a Snellen ratio of 20/200. (top row) Images captured using the DSLR camera with extra lenses varying from 0.0 to -4.0 diopters. (second row) Our simulated results. (third row) SSIM metric results (for each pixel, computed at an 11-by-11 neighborhood). (fourth row) AD metric.

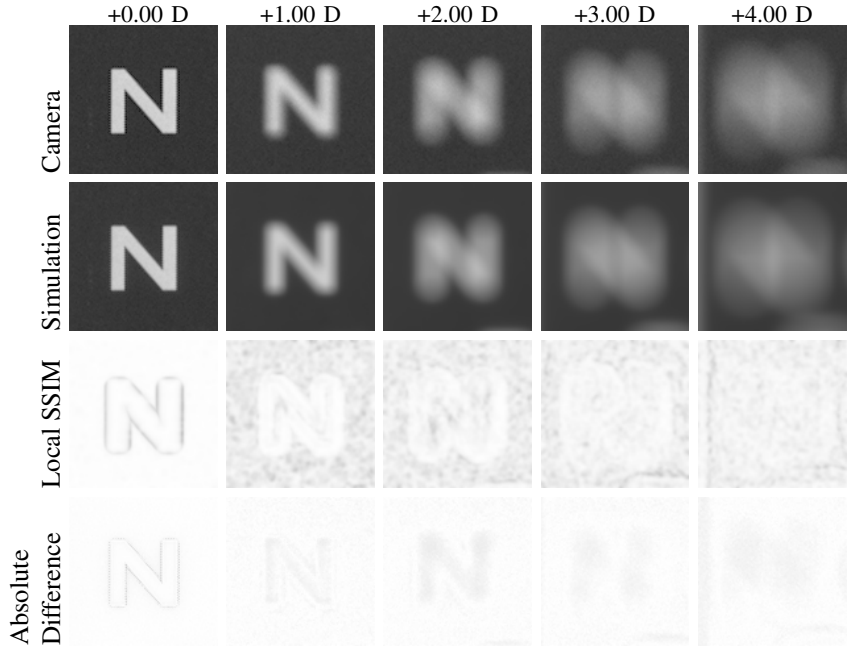

Figure 6. Comparisons of our simulated results against ground truth obtained with a myopic camera. These large images correspond to a Snellen ratio of 20/200. (top row) Images captured using the DSLR camera with extra lenses varying from 0.0 to 4.0 diopters. (second row) Our simulated results. (third row) SSIM metric results (for each pixel, computed at an 11-by-11 neighborhood). (fourth row) AD metric.

simulations were applied to images captured by the camera without any extra lens (*i.e.*, camera +0.00 D). The third and fourth rows of these figures show visual representations of the SSIM an AD metrics, respectively.

Tables III and IV show the numerical results of the SSIM and PSNR metrics for the results presented in Figs. 5 and 6, respectively. Each row represents the value of a specific metric (*i.e.*, SSIM or PSNR) when comparing images captured by the DSLR camera with induced aberration against

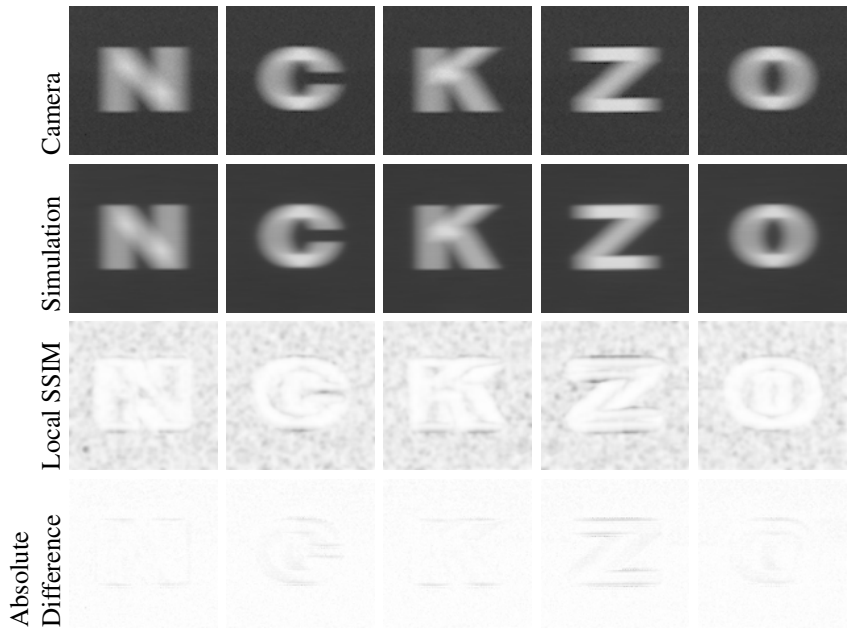

Figure 7. Comparisons of our simulated results against ground truth obtained with a astigmatic camera. These large images correspond to a Snellen ratio of 20/200. (top row) Images captured using the DSLR camera with an extra cylindrical lens with 2 diopters at the vertical meridian. (second row) Our simulated results. (third row) SSIM metric results. (fourth row) AD metric.

the corresponding ones obtained using our simulation. The values of the SSIM metric range from -1.0 (poor similarity) to 1.0 (high similarity). In these tables, one can see that all values are very close to 1.0, indicating that our simulations indeed produces results that are structurally very similar to the ground truth. The PSNR values also indicate that our simulations produce results very similar to the ground truth. Note that PSNR values of 34.0 and above indicate that two images are virtually indistinguishable from each other.

Table III
SSIM AND PSNR TABLE OF THE HYPEROPIC PERCEPTION

	0.00 D	**-1.00 D**	**-2.00 D**	**-3.00 D**	**-4.00 D**
SSIM	0.9869	0.9192	0.9149	0.9119	0.9130
PSNR	34.7778	34.3781	32.8601	32.6680	29.5003

Table IV
SSIM AND PSNR TABLE OF THE MYOPIC PERCEPTION

	0.00 D	**1.00 D**	**2.00 D**	**3.00 D**	**4.00 D**
SSIM	0.9869	0.9378	0.9324	0.9296	0.9322
PSNR	34.7779	38.8748	38.7219	35.6993	39.3720

Besides simulating the effects of defocus (*i.e.*, myopia and hyperopia), we have also compared the results of our simulation for astigmatic vision. This is illustrated in Fig. 7. The Sloan letters in Fig. 7 were captured by the DSLR camera with an additional cylindrical lens with 2.0 diopters, rotated in order to simulate astigmatism in the horizontal meridian ($\phi = 90°$). Table V shows the results of the SSIM and PSNR metrics for these astigmatic results. Again, the SSIM indices are close to 1.0 and the PSNR values are above

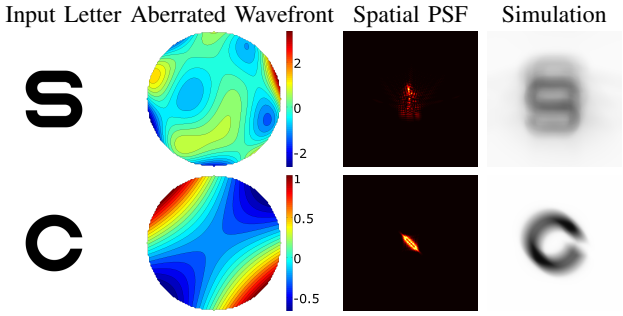

Figure 8. Simulations with arbitrary wavefronts. The input letter images correspond to a Snellen ratio of 20/200. (second column) Normalized aberrated wavefront. (third column) The spatial PSF. (fourth column) Our simulation results given the images shown in column *Input Letter*. The top row shows the results of a simulation involving only higher-order aberrations ($Z_3^{-3} = 0.2$, $Z_3^{-1} = 0.2$, $Z_3^3 = 0.1$, $Z_4^2 = 0.2$, $Z_5^{-5} = 0.4$, $Z_5^1 = 0.3$). The bottom row shows how a combination of low-order aberrations (+0.5 Sph. -2.0 Cyl. at 45) affects the perception of a Sloan letter.

34.00 decibels. Note that for the astigmatic results, part of the differences visible in the astigmatic local SSIM index visualizations (Fig. 7, third row) is due to the difficulty of a precise manual alignment of the astigmatic axes of the additional lens. Any deviation from the simulated angles affects the quality metrics.

Our technique can be used to simulate arbitrary wavefront aberrations, given the corresponding aberration function $W_{(x,y)}$ (Eq. 3). Thus, even though such a validation depends on the existence of an optical ground truth, the method is not limited to what can be modeled using a DSLR camera and

additional lenses. For instance, the top row of Fig. 8 shows simulations of high-order aberrations only. Its bottom row shows how a combination of low-order aberrations (myopia and astigmatism) affects the perception of a Sloan letter.

Table V
SSIM AND PSNR TABLE OF THE ASTIGMATIC PERCEPTION

	N	C	K	Z	O
SSIM	0.9307	0.9271	0.9277	0.9193	0.9303
PSNR	37.2835	35.4130	36.3713	32.7150	36.2564

V. CONCLUSION AND FUTURE WORK

We presented a practical approach for personalized simulation and objective validation of the effects of low-order aberrations on optical systems, such as the human eye. We have demonstrated the effectiveness of our technique by comparing the results of forty simulations against optical ground truths captured by a camera with induced aberrations. For validation, we used three objective metrics: SSIM, PSNR, and the absolute pixelwise differences between the images. For all results, the SSIM values are between 0.91 and 0.987 (mean = 0.93 and standard deviation = 0.02), indicating that our simulations indeed produce results that are structurally very similar to the ground truths. Regarding the PSNR metric, the values vary from 29.50 to 39.37 (mean = 35.50 and standard deviation = 2.14). Such PSNR values, given in decibels, indicate that our simulations are virtually indistinguishable from the optical ground truth captured by a DSLR camera.

Although our solution can take into account high-order aberrations (see Fig. 8, top), we have concentrated our simulations on low-order aberrations. This was intended to avoid the need for expensive wavefront sensors, and to allow validation against ground truth data. As such, we can perform personalized simulations using data directly available from one's eyeglasses prescriptions.

Currently, our technique assumes that all elements of a target scene are at the same known distance from the subject. However, visual aberrations are depth-dependent phenomena. Thus, we would like to capture color and depth information from real environments and generate real-time personalized simulations of how low-order aberrations affect one's perception of such environments.

REFERENCES

[1] Schwartz SH. Visual perception: A clinical orientation. 4 ed.; New York, NY, USA: McGraw-Hill Medical Pub. Div.; 2010.

[2] Dias-Santos A, et al. Higher order aberrations in amblyopic children and their role in refractory amblyopia. Revista Brasileira de Oftalmologia 2014; 73:358-62.

[3] Potmesil M, Chakravarty I. A lens and aperture camera model for synthetic image generation. ACM SIGGRAPH 1981;15(3):297-305.

[4] Barsky BA. Vision-realistic rendering: Simulation of the scanned foveal image from wavefront data of human subjects. In: Proc. 1st Symp. Applied Perception in Graphics and Visualization. 2004, p. 73-81.

[5] Yu WM. Simulation of vision through an actual human optical system. Ph.D. thesis; University of California, Berkeley; 2001.

[6] Camp J, Maguire L, Robb R. An efficient ray tracing algorithm for modeling visual performance from corneal topography. In: Proc. First Conf. Vis. Biomedical Computing, 1990, p. 278-85.

[7] Kolb C, Mitchell D, Hanrahan P. A realistic camera model for computer graphics. In: Proc. SIGGRAPH 95; 1995, p. 317-24.

[8] Mostafawy S, Kermani O, Lubatschowski H. Virtual eye: retinal image visualization of the human eye. IEEE Computer Graphics and Applications,c1997;17(1):8-12.

[9] Krueger, Matheus L. Visual Simulations of Refractive Errors on Monochromatic Images and An Evaluation for the Absolute Threshold for Vision. Masters Thesis, UFRGS, July 2015.

[10] Watson, AB. Computing human optical point spread functions. Journal of Vision 2015; 15(2):26.

[11] Goodman JW. Introduction to Fourier optics. 3 ed.; Englewood: Roberts and Company Publishers; 2005.

[12] Dai Gm. Wavefront Optics for Vision Correction. Bellingham, Washington USA: SPIE PRESS; 2008.

[13] Deering MF. A photon accurate model of the human eye. ACM Trans. Graph. 2005; 24(3):649-58.

[14] Ritschel T, Ihrke M, Frisvad JR, Coppens J, Myszkowski K, Seidel HP. Temporal glare: Real-time dynamic simulation of the scattering in the human eye. Computer Graphics Forum 2009;28(2):183-92.

[15] Pamplona VF, Mohan A, Oliveira MM, Raskar R. Netra: Interactive display for estimating refractive errors and focal range. ACM Trans. Graph. 2010;29(4), 77:1-8.

[16] Kronbauer AL, Schor P, Chamon W, Carvalho LAVd. Vision measurement in candelas: description of a psychophysical technique to quantify luminous intensity. Arquivos brasileiros de oftalmologia 2011;74(2):91-96.

[17] Huang FC, Lanman D, Barsky BA, Raskar R. Correcting for optical aberrations using multilayer displays. ACM Trans Graph 2012;31(6):185:1–12.

[18] Pamplona VF, Oliveira MM, Aliaga DG, Raskar R. Tailored displays to compensate for visual aberrations. ACM Trans. Graph. 2012; 31(4): 87:1–12.

[19] Huang FC, Wetzstein G, Barsky BA, Raskar R. Eyeglasses-free display: Towards correcting visual aberrations with computational light field displays. ACM Trans. Graph. 2014; 33(4):59:1–12.

[20] Montalto C, Garcia-Dorado I, Aliaga D, Oliveira MM, Meng F. A total variation approach for customizing imagery to improve visual acuity. ACM Trans Graph 2015;34(3):28:1-16.

[21] Pamplona VF, Oliveira MM, Baranoski GVG. Photorealistic models for pupil light reflex and iridal pattern deformation. ACM Trans. Graph. 2009; 28(4):106:1-12.

[22] Pamplona VF, Passos EB, Zizka J, Oliveira MM, Lawson E, Clua E, et al. Catra: Interactive measuring and modeling of cataracts. ACM Trans. Graph. 2010; 30(4), p. 47:1-8.

[23] Machado GM, Oliveira MM, Fernandes LA. A physiologically based model for simulation of color vision deficiency. IEEE TVCG 2009;15(6):1291-8.

[24] Bailey I, Lovie J. New design principles for visual acuity letter charts. American Journal of Optometry and Physiological Optics 1976;53(11):740-745.

[25] Pelli D, Robson J, et al. The design of a new letter chart for measuring contrast sensitivity. In: Clinical Vision Sciences. Raphaels Ltd; 1988.

[26] Glytsis EN. Example of a simple optical system; 2014. URL: http://http://users.ntua.gr/eglytsis/OptEng/Two_Lenses_Example.pdf.

[27] Wang Z, Bovik A, Sheikh H, Simoncelli E. Image quality assessment: from error visibility to structural similarity. IEEE Trans. on Image Processing, 2004;13(4):600-12.